Interannual changes of the summer circulation and hydrology in the East China Sea: A modeling study from 1981 to 2015

Yi-Chun Kuo [a], Yang Yu [b], Yu-Heng Tseng [a,c,*]

[a] *Institute of Oceanography, National Taiwan University, Taipei, Taiwan*
[b] *Key Laboratory of Ocean Circulation and Waves, Institute of Oceanology, and Center for Ocean Mega-Science, Chinese Academy of Sciences, Qingdao, China*
[c] *Ocean Center, National Taiwan University, Taipei, Taiwan*

ARTICLE INFO

ABSTRACT

This study investigated long-term interannual changes in summer circulation and hydrology in the East China Sea (ECS) by performing 35-year high-resolution ocean model simulation from 1981 to 2015. The sea surface temperature (SST) warming trend was considerably weaker in summer than in winter. To the east of the Yangtze Estuary, the interannual variation of SST in summer was mainly dominated by horizontal advection associated with variations in the Taiwan warm current and heat flux in the offshore region north of the Yangtze Estuary. Baroclinic circulation during summer played a crucial role in subsurface mixing. Near the surface, the significant atmospheric wind mode (EOF1) and Kuroshio mode (EOF2) dominate interannual variations in ocean circulation. In the subsurface, local wind around the Tsushima Strait dominated the interannual ocean variation. Anomalous northeasterly winds induced a southwestward pressure gradient due to topographical confinement. These anomalies propagated to the south along the continental shelf through topographic Rossby waves. This study identified two types of anomalous features based on combinations of surface and subsurface EOFs. The combination represents an in-phase contribution between wind and Kuroshio forcings and between the surface and subsurface circulation that enhances the hydrological variability in the ECS. The implication on the relevant biogeochemical and ecological studies in the East China Sea is also very crucial at the interannual time scale.

1. Introduction

The East China Sea (ECS) is located at the mid-latitudes of the northwestern Pacific. It is surrounded by mainland China, Taiwan, Ryukyu and Kyushu Islands, and the Korean Peninsula. The continental shelf region that is shallower than 200 m accounts for approximately 66% of the ECS (Fig. 1). To the south of the ECS, the Taiwan Strait connects the ECS to the northern South China Sea. To the north of the ECS, the Tsushima Strait connects the northern ECS with the Japan Sea. Over and beyond the shelf break, the northward-flowing Kuroshio mostly follows isobaths.

The ECS is among the largest marine ecosystems in the world. In summer, the southwesterly monsoon wind (Fig. 1) causes the circulation to flow northeastward (Liu and Gan, 2014), thus facilitating the northward intrusion of the Taiwan Warm Current (approximately 1.2–1.3 Sv) driven by the large-scale pressure gradient (Yang, 2007). The intrusion of Kuroshio waters (approximately 1.3–1.4 Sv) from the shelf break is a characteristic of the bottom water of the ECS shelf (Zhou et al., 2018) that regulates its biogeochemical processes (Zuo et al., 2019; Chen et al., 2020; Zhai et al., 2020). The Yangtze River

(Changjiang) discharges substantially high concentrations of anthropogenically derived nutrients into the ECS. In addition, the shelf current and tidal mixing play crucial roles in exporting the river plume (Rong and Li, 2012). The discharged water creates a buoyant plume that traps solar radiation, thus enhancing vertical stratification through positive feedback. During July and August, when the Yangtze River discharge peaks, the upwelling generated by the horizontal divergence of the Yangtze River plume drives the upward movement of nutrients from the bottom water (Chen, 2000; Isobe and Matsuno, 2008).

In the ECS, the Kuroshio is the most energetic current. It flows northeastward along the 200-m isobaths. The subsurface Kuroshio water may intrude into the ECS shelf through three pathways: (1) over the shelf off the northeast of Taiwan, (2) over the central slope of the ECS, and (3) over the shelf off the southwest of Kyushu (Liu et al., 2021a). The intrusion off northeastern Taiwan is established through a spiral structure of velocity associated with the topographic effect caused by the induction of uplift velocity by the along-shore variation in slope (Yang et al., 2018). This phenomenon facilitates the intrusion of subsurface Kuroshio into the ECS. The intrusion structure is altered due to variations in the Kuroshio intensity, baroclinicity and local wind
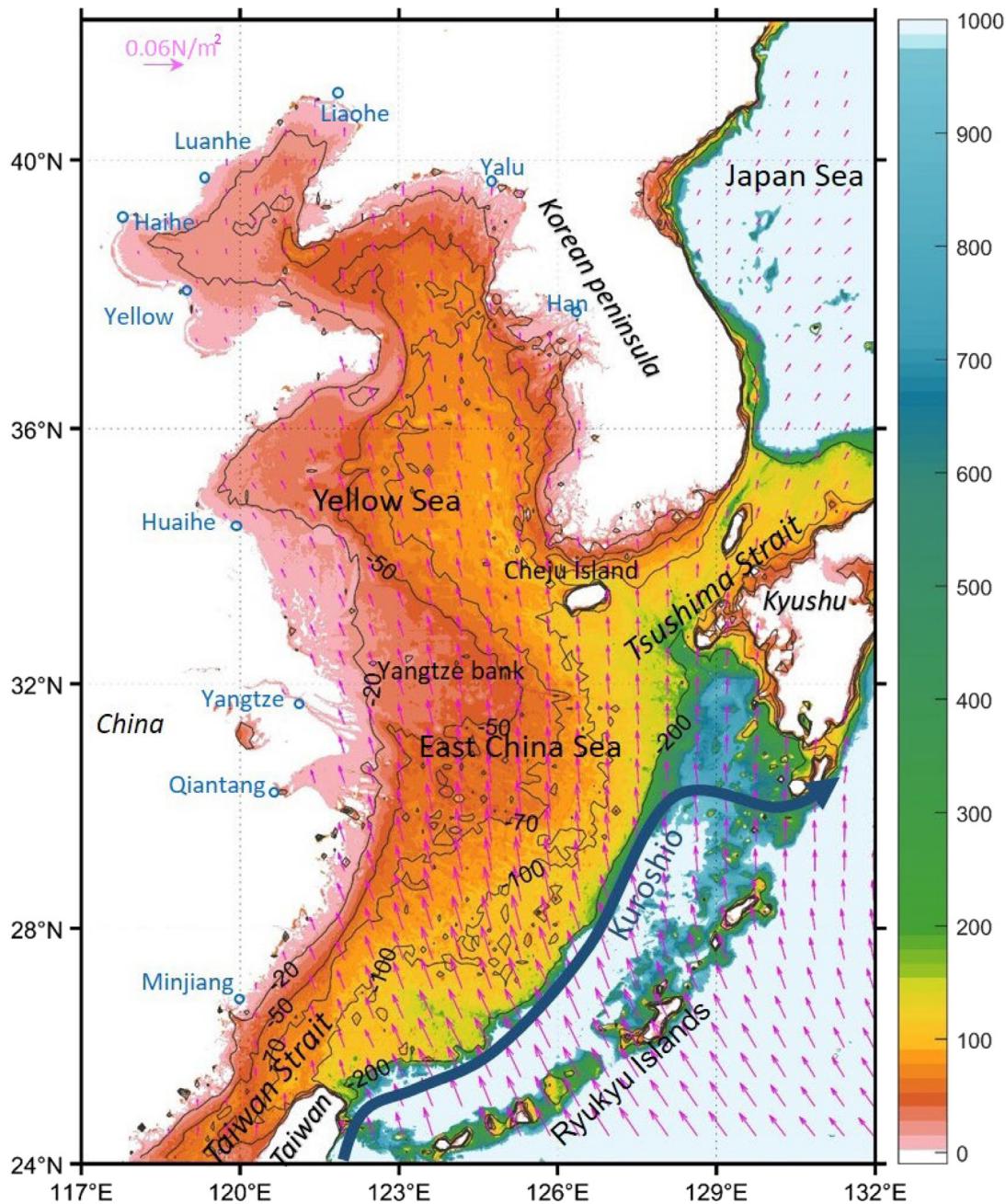

Fig. 1. The model domain and topography (m). Magenta vectors show the climatological surface wind stress (N/m^2) during July.

stress (Liu et al., 2021b). Over the central slope of the ECS, the Kuroshio intrusion is determined by the along-shore pressure gradient (cross-shore geostrophic current), which is attributed to the joint effect of baroclinicity and relief (JEBAR) and the bottom stress curl (Guo et al., 2006). The intrusion varies with depths, presenting a multiple-layered pattern in the water column between 100- and 200-m isobaths. Overall, the intrusion is stronger in the subsurface (>50 m) than in the surface (Zhang et al., 2017).

In the last four decades, significant surface warming has been observed in the ECS during winter due to the wind-induced spreading of the Kuroshio warm water in addition to the air–sea heat flux (Oey et al., 2013). During summer, because the surface Kuroshio intrusion is nearly absent (Zhang et al., 2017), the warming trend is insignificant (Wang et al., 2013; Sasaki and Umeda, 2021). In terms of interannual variability, Kuroshio transport in the continental shelf of ECS is associated with large-scale climate variability, including modulation related to the El

Niño–Southern Oscillation (ENSO) (Liu et al., 2014) and Pacific decadal oscillation (Andres, 2008; Soeyanto et al., 2014). In the Taiwan Strait, the interannual variability of volume transport is mainly driven by the East Asian summer monsoon (Hong et al., 2009).

In the inner shelf region of the ECS, interannual changes in circulation substantially affect the marine ecosystem. Xu et al. (2019) observed significant interannual variability in phytoplankton communities within the ECS ecosystem during summer in response to an increase or decrease of the Kuroshio water. Although several studies have discussed the interannual variability of the Kuroshio, Taiwan Strait current, and Asian monsoon, interannual variations in the inner shelf of the ECS and its dynamics have rarely been addressed. The relative contribution of local forces (winds stress, winds stress curl and riverine discharge) and remote forces (the Kuroshio intrusion and Taiwan Strait inflow) to interannual variations in ECS circulation remains unclear. In this study, we performed a 35-year high-resolution ocean
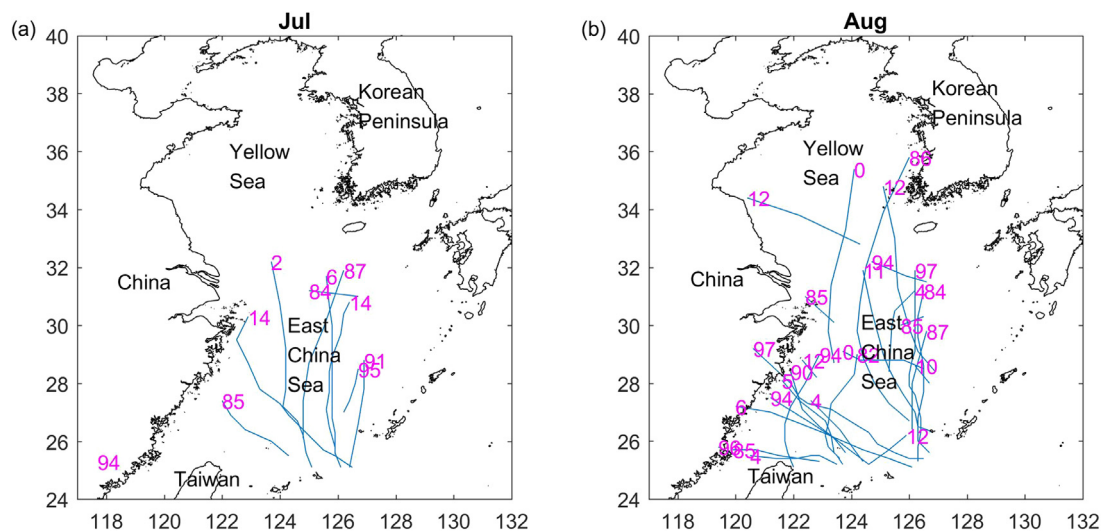
Fig. 2. The historical typhoon tracks during (a) July and (b) August between 1982 and 2015. Individual years are labeled. The best track typhoon data were retrieved from the Japan Meteorological Agency (JMA) (https://www.jma.go.jp/jma/jma-eng/jma-center/rsmc-hp-pub-eg/trackarchives.html).

model simulation to investigate long-term variations in the ECS during summer. This study identifies the dominant interannual modes in the summer ECS for the surface and subsurface, respectively. These results will impact our current understanding of the regional ocean climate study in the ECS due to the different feedbacks for the surface and subsurface (baroclinicity). Section 2 introduces the numerical model. Section 3 presents a validation of the model results on the basis of observations. Furthermore, long-term trends and interannual variability are addressed. Section 4 confirmed and concluded the relative importance of the local and remote forcings on the two dominant types of anomaly features based on a sensitivity experiments. Finally, Section 5 provided our summary.

2. Numerical model and observation

The 35-year ECS simulation performed in this study was based on the Regional Ocean Model System model integrated from January 1981 to December 2015. This model configuration efficiently simulated diurnal and seasonal temperature and salinity variations in the ECS (Yu et al., 2017a,b, 2020). The model domain ranges from 24°N to 41.3°N and from 117°E to 132°E (Fig. 1) with a horizontal resolution of 1/18° (~6 km). The model has 30 "S layers" in the vertical direction and uses the double stretching function reported by Shchepetkin and Mcwilliams (2009) to achieve a higher model resolution at the surface.

The model simulation was initialized on January 1, 1981, on the basis of Simple Ocean Data Assimilation Version 3 (SODA3) reanalysis data for sea surface height (SSH) and velocity fields (Carton et al., 2018). Information on temperature and salinity was obtained from the January climatology of the World Ocean Atlas 2013 (Locarnini et al., 2013; Zweng et al., 2013). Pentad SODA3 reanalysis data with a resolution of 1°/4° (~27 km) were used as the lateral boundary conditions of SSH, currents, temperature, and salinity for consistency. Ten principal tidal constituents—M2, S2, N2, K2, K1, O1, P1, Q1, Mf, and Mm (harmonic constants for tidal elevation and currents)—derived from the Oregon State University global inverse tidal model of TPXO7.0 with a nodal correction (amplitude and phase adjustments of harmonic tidal constituents over an approximate 18.61-year cycle), are specified as tidal forcing at the lateral boundary (Egbert et al., 1995; Egbert and Erofeeva, 2002). Different boundary conditions are used for SSH (Chapman type, Chapman, 1985), barotropic velocity (Flather type, Flather, 1976), and temperature/salinity (Orlanski-type radiation condition; Orlanski, 1976), respectively.

The 6-hourly National Center for Environmental Prediction/ National Center for Atmospheric Research reanalysis data were used

to provide atmospheric forcing data (Kalnay et al., 1996), including wind speed (10 m), solar radiation, air temperature (2 m), air pressure (2 m), precipitation rate, cloud fraction, and relative humidity. Solar insolation uses a double exponential absorption function with Jerlov water type II parameters (Paulson and Simpson, 1977). Radiative cooling caused by longwave radiation was calculated using the Berliand algorithm (Berliand, 1952). The latent heat, sensible heat, and wind stress were computed using COARE 3.0 bulk formulas (Fairall et al., 1996, 2003). The "cool skin" effects on sea surface heat and vapor fluxes were determined using an empirical correction scheme (Fairall et al., 1996).

The 10 largest rivers were included within our model domain (Yangtze, Yellow, Huaihe, Liaohe, Haihe, Luanhe, Minjiang, Qiantang, Yalu, and Han rivers, Fig. 1). The monthly mean river discharge data were derived from the Global River Discharge Project (http://daac.ornl.gov/RIVDIS/rivdis.shtml) (Vorosmarty et al., 1998). The diluted riverine water was discharged into all model layers (30 layers) at the upstream region of the river with 0 psu. The river temperature was determined using climatological monthly SODA3 data. The interannual change in river discharge was not considered in the present study; this change may alter ECS circulation at some points.

During July and August, the area and volume of the Yangtze River plume peak and the summer flow pattern reached a matured phase. We selected July in this study to reduce complexity, given that a large number of typhoons with diverse trajectories occurred in the ECS during August 1982–2015 (Fig. 2). On average, the ECS is impacted by 4 typhoons annually (Chen et al., 2017). The number of typhoon events is less than that in the South China Sea, but these typhoons are often more powerful in the ECS (Chen et al., 2017). When two or more typhoons pass by continuously within a month, significant ocean response to typhoons will be quite complicated for the analysis owing to the large air–sea momentum and energy flux exchanges. These events need to be studied individually so that we exclude August from the present study. For ocean data, high-resolution optimum interpolation SST (OISST) from the NOAA National Climatic Data Center was used for the period from 1982 to 2015 (https://www.psl.noaa.gov/data/gridded/data.noaa.oisst.v2.highres.html). We used HYCOM (HYbrid Coordinate Ocean Model) reanalysis data (GOFS3.0 and GOFS3.1) to validate our model results because *in-situ* and satellite ocean measurements have been assimilated in HYCOM. In addition, the CTD data in a region between 122°E–126°E, and 28°N–32°N collected by the research vessels Ocean Researcher I, II, III during the cruise in July between 1997 and 2014 is used to validate the model results. The data
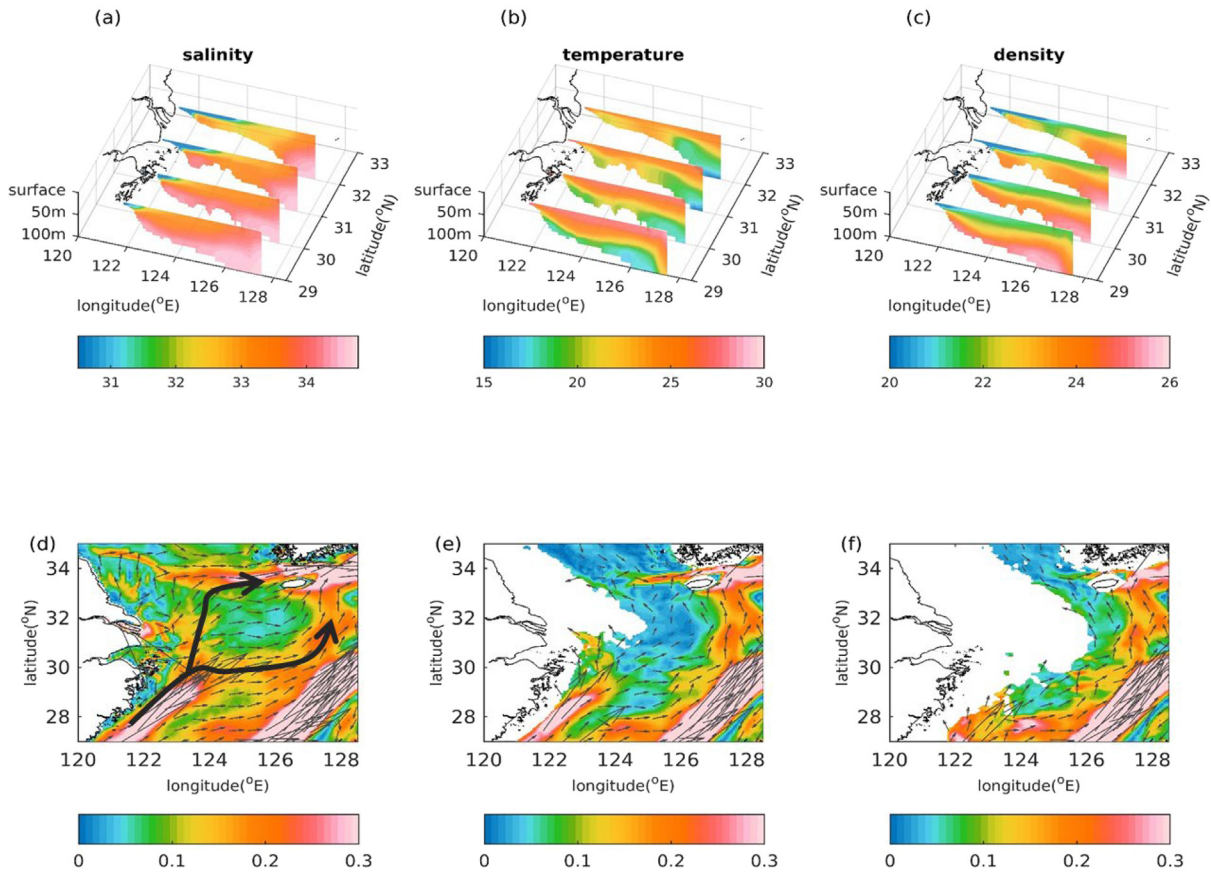
Fig. 3. (a) 35-yr mean climatology of salinity (psu) at four latitudes (30°N, 31°N, 32°N and 33°N). Surface distribution is shown as contours. (b) and (c) same as (a) but for temperature (°C) and density (σ), respectively. (d)–(f) mean circulation and current speed (m/s) at 10 m, 40 m, and 70 m during July, respectively. Thick black arrows in (d) show the flow divided into two branches due to the Yangtze bank.

is provided by the Ocean Data Bank of National Science and Technology Council (http://www.odb.ntu.edu.tw/).

We conducted an empirical orthogonal function (EOF) (Kutzbach, 1967) analysis and the linear regression of environmental variables (e.g., SSH, currents, wind stress, wind stress curl, and surface heat flux) on EOF modes by the least squares method (Emery and Thomson, 2001). The surface heat budget (Eq. (1)) is used to explain these EOF modes. In Eq. (1), the horizontal dissipation is negligible and the vertical diffusion term can be viewed as the difference between the net surface heat flux and the turbulent heat flux at the bottom of the ocean surface layer. Base on the EOF results, an addition numerical experiment, Exp1, is conducted. In Exp1, the ocean states (initial and boundary conditions) during 2009/6/1-2009/7/31 is forced by the atmosphere states during 2014/6/1-2014/7/31. This will be further addressed in Section 4.

$$
\underbrace{\frac{\partial T}{\partial t}}_{tendency} = -\underbrace{\left(u\frac{\partial T}{\partial x} + v\frac{\partial T}{\partial y} \right)}_{horizontal\ advection} - \underbrace{w\frac{\partial T}{\partial z}}_{vertical\ advection} - \underbrace{\frac{\partial}{\partial z}\left(k\frac{\partial T}{\partial z} \right)}_{vertical\ diffusion}
$$
$$
+ \underbrace{\{F + D\}}_{forcing\ and\ horizontal\ dissipation} \tag{1}
$$

3. Model results

3.1. Model verification and climatology

Fig. 3 presents 35-year averaged depth-longitude salinity, temperature, and density profiles in the ECS and the flow field at depths of 10, 40, and 70 m. At the surface, the spatial variation in density was dominated by the diluted water of the Yangtze River, causing a minimum to

the west near the river mouth (Fig. 3a, c). In the subsurface, the ocean temperature and salinity were determined by the Taiwan warm current and Kuroshio intrusion. Off the China coast, the isotherm elevated onshore, indicating the typical upwelling phenomenon (Fig. 3b). At deeper depths, cold water (<15 °C) appeared at approximately 33°N and 126°E, where the minimum flow velocity (around the center of cyclonic circulation) was observed. The cold water in the bottom region is formed during wintertime transported by the southward cross-shelf circulation in the Yellow Sea and ECS (Yuan and Hsueh, 2010). The cold water distribution in Fig. 3b and d is similar to the climatologically averaged data reported by Johnson et al. (2015, Figure 4.5). The northward subsurface flow at around 32°N and 124°E–125°E divided into two branches where bottom topography rises (i.e., encountering the Yangtze bank). One branch flows cyclonically around the bank and the other flows across the west side of the bank (Fig. 3d). A large density gradient was noted in the subsurface on the east and west flank of the Yangtze bank, depicting clear frontal structures in the shallow water where baroclinicity and significant velocity shear appeared. Near the surface, the northward current from the Taiwan Strait turned eastward when it reached the Yangtze bank. Subsequently, the northward current flowed cyclonically and entered the Japan Sea through the Tsushima Strait. In the subsurface, significant Kuroshio intrusion was noted in regions at approximately 123.5°E and 127.5°E.

Fig. 4 shows the CTD data collected by the research vessels Ocean Researcher I, II, III during the cruise in July between 1997 and 2014. Based on the distribution of these CTD stations, we choose three areas (M1, M2, and M3 as shown in Fig. 4) to compare the mean CTD temperature profiles and the mean model results. The correlation coefficient between the interannual variation in the CTD data and model at different depths in the area of M1, M2, and M3 are shown
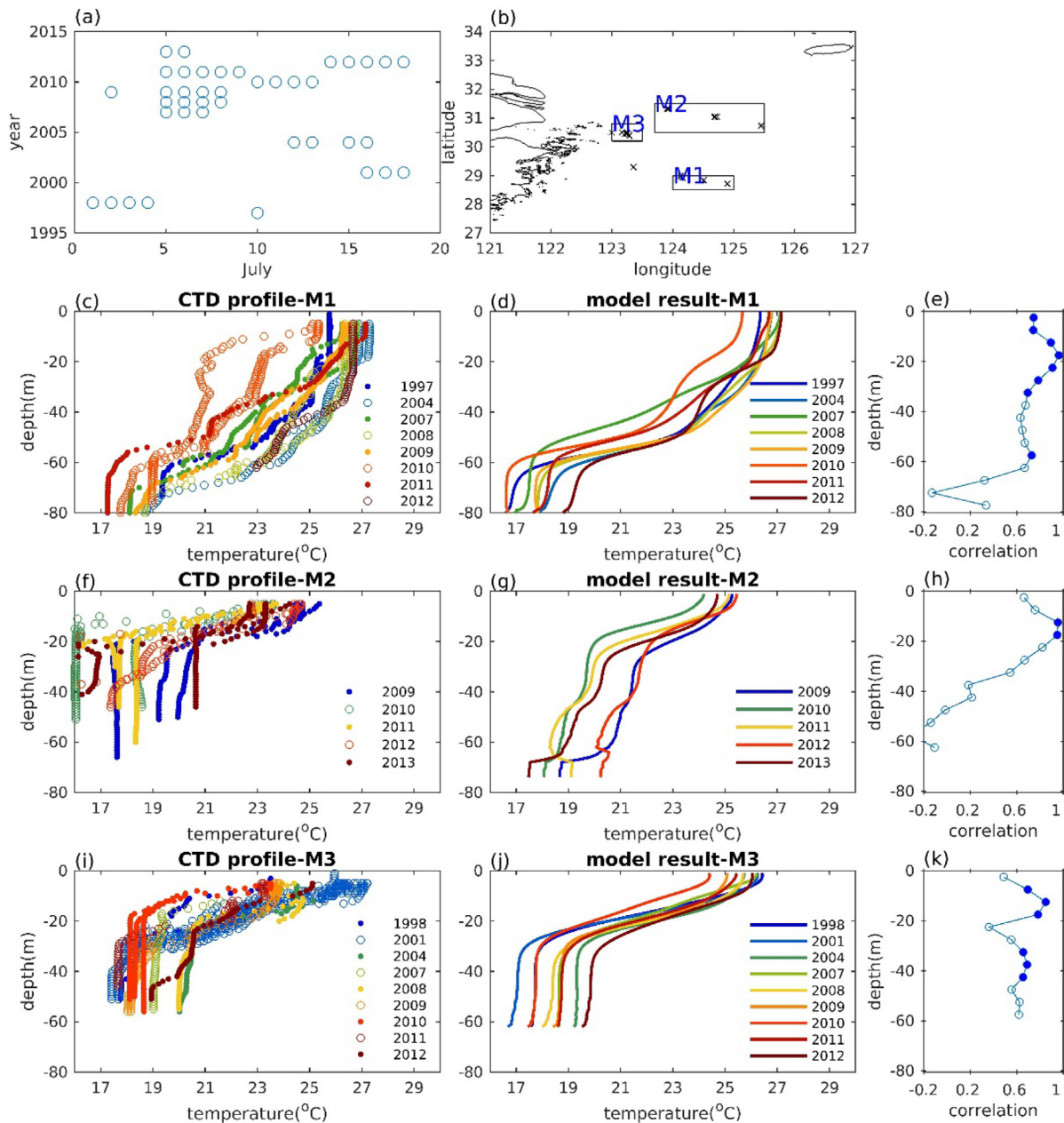
Fig. 4. (a) The CTD data collected by the research vessels Ocean Researcher I, II, III during the cruise in July between 1997 and 2014. (b) Location of the CTD stations and the M1, M2 and M3 regions. The mean temperature profile in M1 region from (c) the CTD data and (d) model. (e) Correlation between the interannual variation in the CTD data and model in M1. The solid circles indicate significant at the 5% level. (f)–(h) are the same as (c)-(e) but for M2 region. (i)-(k) are for the region.

in Fig. 4e, h, and k, respectively. Overall, the model shows similar interannual variation to the observations. We note that we do not expect the model results can exactly match the CTD data due to the lack of data assimilation. The changes in the observation are larger than the model monthly-mean results. The model results are compared well with the CTD temperature profiles in M1 and M3. The simulated temperature below 20 m is slightly higher in M2. However, the thermocline depth is well presented in the model.

We also compared the 35-year modeled ocean temperature and SSH during July with OISST and HYCOM reanalyses (Fig. 5). The modeled SST pattern was consistent with the OISST. The biases were less than 0.5 °C in most domains (Fig. 5b). However, some deviations were larger than 1 °C in the shallow (<20 m) coastal region north of the Yangtze Estuary. The discrepancy is partly due to imperfect surface forces such as freshwater runoff and the high-frequency diurnal winds in this region. The model SST exhibited the maximum standard deviation to

the south of Cheju Island where a cyclonic circulation was located. This feature was also noted in the OISST (figure not shown). The modeled time series of SST was consistent with the variation of OISST as the correlation coefficient is larger than 0.8 in most domains, indicating that the simulations were reliable for interannual SST variability (Fig. 5c).

Previous observations showed that the summer mixed layer depth was approximately 20 m in the study region (Du and Liu, 2017; Moon et al., 2019). This is consistent with the CTD results in M1. For the shallower regions (M2 and M3), the thermocline depth is around 20 m and 30 m, respectively. Thus the subsurface depth is defined as 30–70 m in the study region. The comparisons in mean subsurface temperature between HYCOM and our model during 1994–2015 are shown in Fig. 5d–f. The comparison of the subsurface temperature shows larger biases (Fig. 5e) than in the surface, especially in the boundary region between ECS and the Yellow Sea and off the northeast of Taiwan. However, our modeled time series correlated well with the
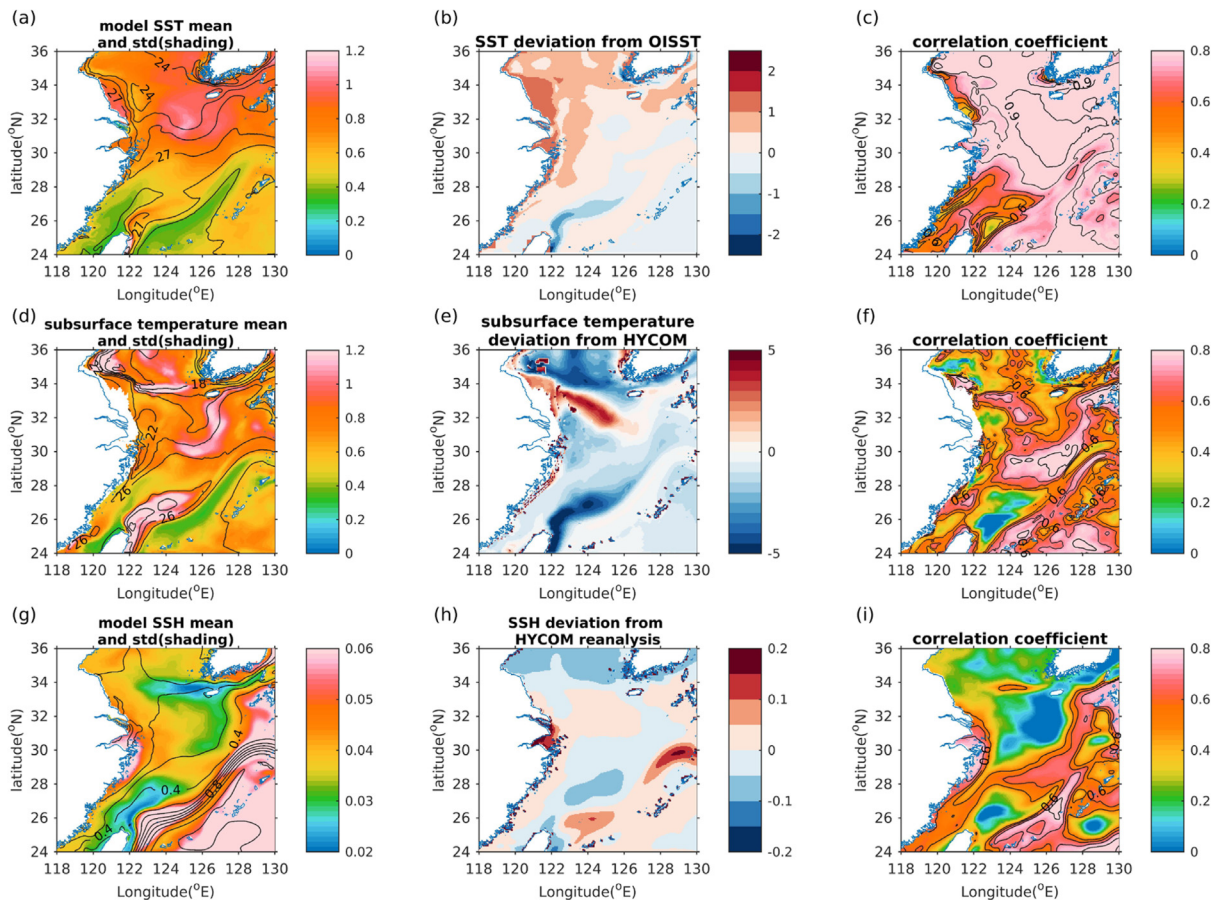
Fig. 5. (a) modeled SST mean (contours) and standard deviation (shading) during 1982–2015. (b) the modeled SST deviated from the OISST (°C). (c) correlation between the modeled SST and the OISST (black contours have the interval of 0.15 and p < 0.05). (d)–(e) is same as (a)–(b) except for the subsurface (30–70 m) temperature (°C), and (f) is the correlation with HYCOM reanalysis (1994–2015) (black contours have the interval of 0.15 and p < 0.05). (g)–(i) are the same as (a)–(c) except for the modeled SSH (m) and its deviation from the HYCOM reanalysis (1994–2015).

HYCOM reanalysis in most of the region except off the northeast of Taiwan (Fig. 5f). Particularly, the similarity in the central and northern ECS suggests that our analysis in these regions is reliable.

Studies have rarely performed long-term direct current measurements in the ECS. Ocean circulation can be deduced from stratified ocean temperature and SSH, which include both baroclinic and barotropic components (Goni et al., 1996). Furthermore, we compared the modeled SSH with HYCOM data in this subsection. The modeled SSH was generally higher in the Kuroshio region and gradually decreased toward the west as expected. In addition to the Kuroshio region, the standard deviation was higher along the China coast, possibly due to variations in the anomalous wind-induced coastal flow (Fig. 5g). The modeled SSH correlated well with HYCOM reanalysis in most domains except the inner portion of cyclonic circulation south of Cheju Island and off the northeast coast of Taiwan, where a cyclonic eddy existed during summer (Fig. 5i). These low correlation regions are partly attributable to large interannual variability locally.

3.2. Long-term trends

The variability of SST in the ECS is mainly driven by the oceanic advection and air–sea heat flux (Cai et al., 2017). Fig. 6 presents the spatial distribution of long-term trends for SST during 1981–2015: (a) annual mean and (b) July. SST warming was mainly observed in the southwestern ECS (north of Taiwan; Fig. 6a and b). The spatial distribution of the linear trend of the annual mean SST suggested a slight warming trend (approximately 0.02 °C/y; Fig. 6a); this finding is similar to OISST results for the period 1982–2017 reported

by Wang et al. (2019). However, the modeled warming trend was weaker than that reported by Wang et al. (2019) off the China coast, where the warming trend reached 0.03–0.04 °C/y. This difference may be attributed to two main reasons. The first is the shift of the climatological initial condition in our simulation. The second is that the coarse resolution atmospheric force cannot exactly depict land–sea differences along the coast, thus causing potential heat flux biases. The summer SST warming was not evident in the ECS in the observation (Fan et al. 2013, Sasaki and Umeda, 2021). Moreover, no clear warming trend was observed for most of the ECS region in July in the model simulation (Fig. 6b). Fig. 6c and d show the corresponding time series of annual mean and July SST, respectively. We separated the time series before and after 1998 because the well-known global warming hiatus started in 1998 and ended in 2012 (Medhaug et al., 2017). For the annual-mean SST, the ECS warming trend before and after 1998 was approximately 0.031 °C/y and −0.039 °C/y, respectively. However, the July SST trend before 1998 was −0.01 °C/y. After 1998, the SST trend decreased to −0.02 °C/y. Despite the nonsignificance of the long-term trend in SST in summer, a considerable interannual variation in summer SST was noted (Fig. 5a), especially in the inner shelf region. This variation was further discussed in the following section.

Subject to the global warming, the upper layer of Kuroshio was speculatively intensified due to the sea surface warming and changes in the basin scale wind stress curl (Cheon et al., 2012; Sakamoto et al., 2005). Acceleration of the Kuroshio in the ECS was observed in the *in-situ* hydrographic data for the period of 1955 to 2010 (Wei et al., 2013). During the warming hiatus (1998–2013), the Kuroshio exhibited a weakening trend (Liu et al., 2021). Fig. 7 presents the Kuroshio mean speed and long-term linear trend of speed during 1981 to 2015 and the
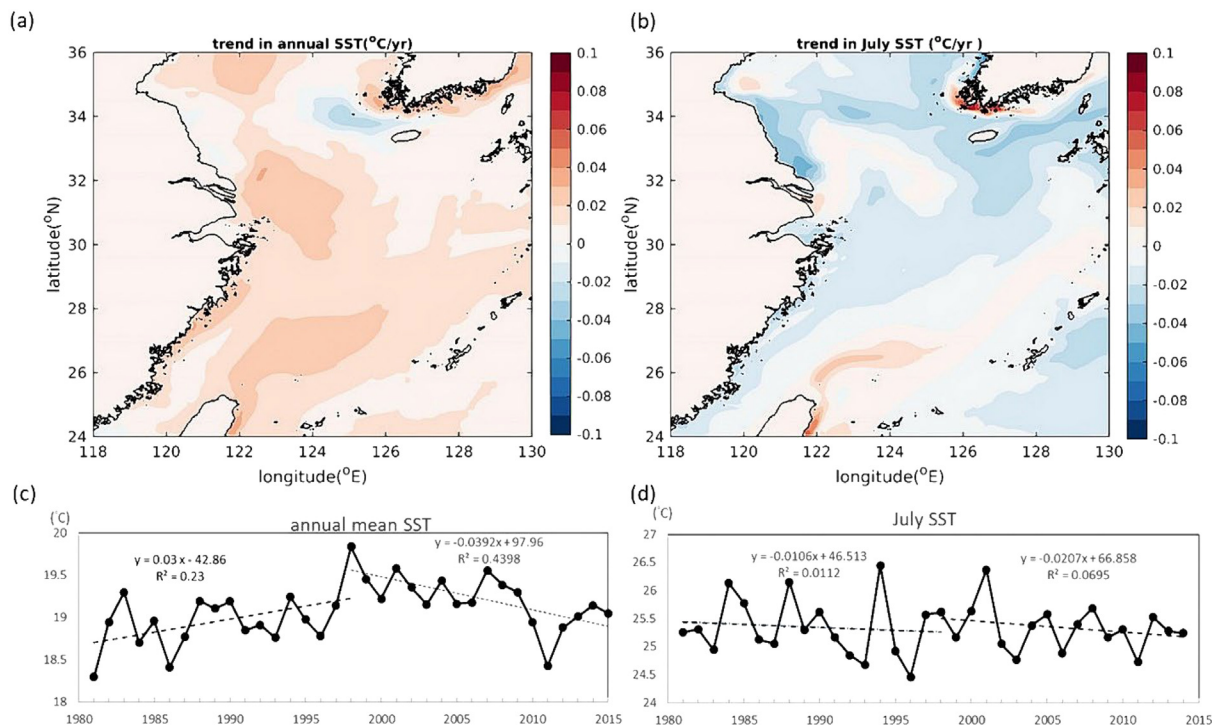
Fig. 6. Linear trend of (a) annual SSTs (°C/yr.) (b) July SSTs (°C/yr.). (c) Time series of annual-mean SST. Linear trends before and after 1998 are also shown. (d) same as (c) but for July.

linear trend during the global warming hiatus for yearly mean speed and July mean speed, respectively. The 35-year long-term trend of the annual Kuroshio speed was mostly positive along the main stream, except it exhibited an off-shelf shift between 127°E and 130°E (Fig. 7b). The increasing trend was stronger during summer (Fig. 7e), and it led to weakened subsurface intrusion for an enhanced cross-shelf pressure gradient (Guo et al., 2006). During the hiatus period, the yearly mean exhibited a weakening trend (Fig. 7c). For the July result, the linear trend during the warming hiatus was similar to the long-term trend during 1981 to 2015. The difference in the behavior between yearly mean and July data might be associated with seasonal variations in the basin-scale wind anomaly or variations in the northwestern Pacific. Additional studies are required to determine the cause of this difference but beyond the scope of this work.

3.3. Interannual variation

3.3.1. The surface

Fig. 8 presents the first EOF (EOF1) and its associated principal component (PC1) using mean data in July for the interannual summer SST variation (accounts for 66% of total variance). The second and third modes contributed to less than 7% of the total variance, which is regarded as noise. EOF1 exhibited a spatially coherent in-phase pattern, with the maximum observed in the northern ECS. Fig. 8c illustrates the linear regression maps of PC1 against surface heat flux (shading, downward flux was positive), wind stress (red vectors), and surface flow (black vectors). The regression results revealed an association between EOF1 and the heat flux around the offshore region north of the Yangtze Estuary (marked by black "A" in Fig. 8) and the northeastward current south of the Yangtze bank.

We used a surface heat budget equation to explain how different processes contribute to interannual SST variations in the ECS (Eq. (1)). Because the SST variance in most of the EOF region was not significantly associated with local heat flux (Fig. 8c), the vertical diffusion and the force terms were not dominant. In Fig. 8c, the northeastward current off the China coast south of the Yangtze bank brings warm

horizontal advection as the current (velocity vectors) heads toward a direction of negative temperature gradient (black contours in Fig. 5a). The heat flux variation in region "A" contributed to oceanic heat advection. Heat flux anomalies in region "A" were not significantly correlated with their surrounding values and local wind stress. We investigated the spatial distribution of the interannual surface heat flux variation during summer. Fig. 9 presents the standard deviation of the modeled surface sensible heat flux, latent heat flux, shortwave radiation, longwave radiation, and net heat flux. Both the latent heat flux and shortwave radiation dominated the net heat flux variation because the other two terms had relatively small contributions. The large interannual variation in shortwave radiation is attributable to the strong adiabatic descent motion with increased downward solar radiation resulting from anomalous anticyclonic circulation over northwestern Pacific (Cai et al., 2017; Tan and Cai, 2018). The net heat flux variability revealed the local minimum at approximately 124°E–126°E and 31°N–33°N, where the maximum EOF1 of SST was observed. This finding is attributable to the out-of-phase relationship between the latent heat flux and shortwave radiation, as indicated by the negative correlation (less than −0.7) in Fig. 9e. In the shallow region north of the Yangtze Estuary (marked "A"), the absence of the negative correlation between the latent heat flux and shortwave radiation caused a large variability in the net surface heat flux. This might be due to the presence of a moisture source from the land region. A recent study suggested that soil moisture anomalies in the Yangtze River valley may significantly modulate the sensible and latent heat flux in the offshore region (Zuo and Zhang, 2016). This SST change associated with variations in the heat flux could control the EOF1 of the SST pattern through the oceanic advection process.

Fig. 10a–d presents the first two dominant EOFs and their associated PCs for surface currents outside of the Yangtze Estuary, where the subsurface temperature and SSH agreed with HYCOM reanalysis data (Fig. 5). The EOF domain was chosen based on the region of inner shelf circulation, excluding the Kuroshio main stream. These two dominant modes explained up to 60% of variance. EOF1 represented coastal current anomalies, and EOF2 depicted cyclonic circulation approximately
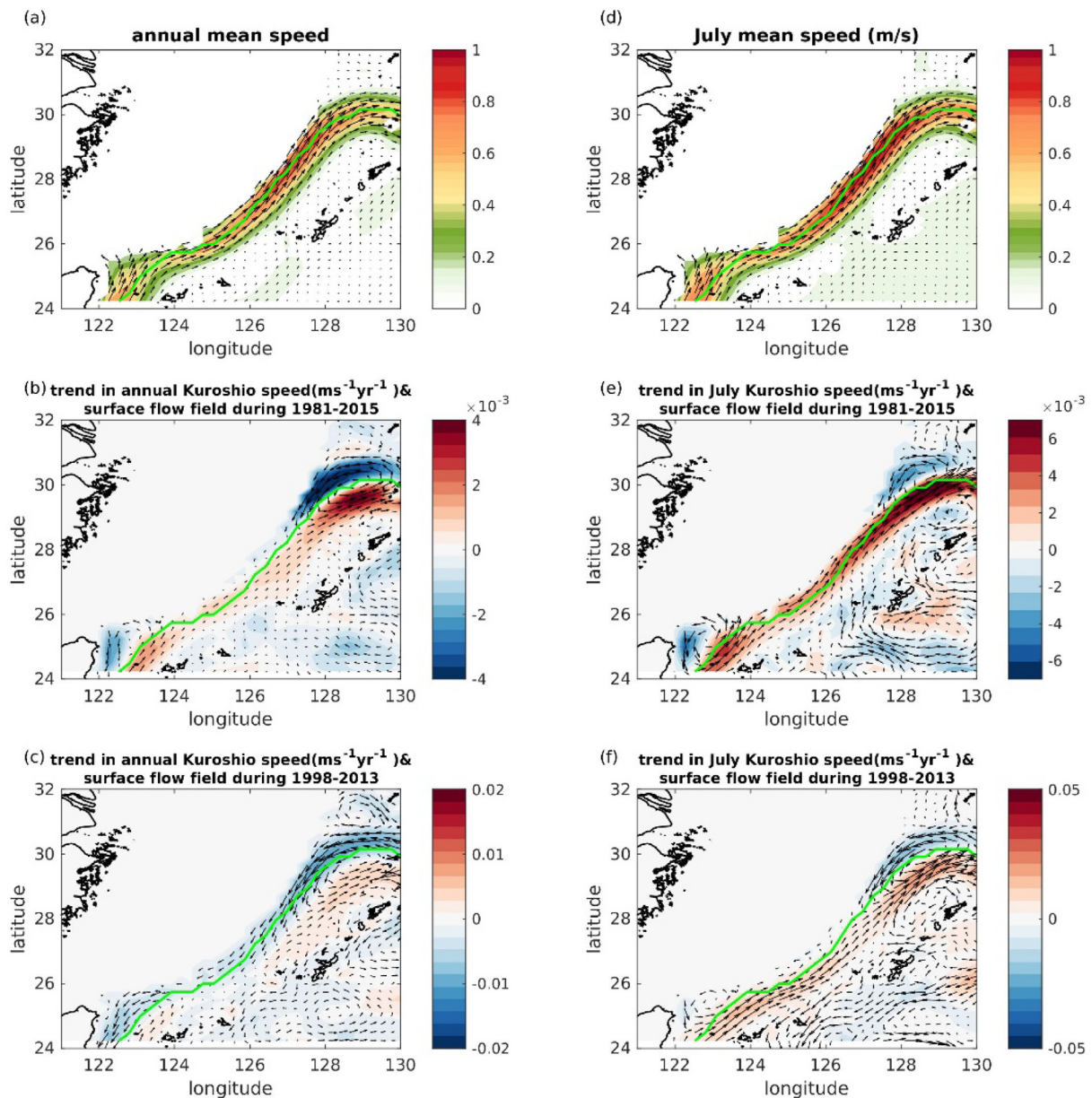
Fig. 7. (a) Annual Kuroshio mean speed (<200 m, m/s), and linear trend in annual Kuroshio speed (ms^{-1}yr $^{-1}$) and flow field (b) during 1981–2015 and (c) during 1998–2013 (the global warming hiatus). The green lines shows the Kuroshio main stream (defined by the max current speed). (d)–(f) are the same as (a)–(c) except for July.

along 70-m isobaths, indicating that the surface current EOFs have a subsurface feature. These two patterns suggest two potential modes affecting the summer SST variation: the atmospheric wind (atmosphere forcing) mode and Kuroshio (ocean inherent) mode, respectively. The regression maps depicted in Fig. 10e suggest that the EOF1 pattern of surface flow is attributed to the strength of the East Asian summer monsoon over the ECS (Fig. 1). Years of positive PC1 are associated with anomalous northeasterly wind over the central and northern ECS. The wind stress anomalies associated with weakening of the summer monsoon around the Yangtze Estuary region induces horizontal convergence accompanying with positive SSH anomalies along the China coast (Fig. 10e). Changes in Kuroshio were not significantly related to EOF1. By contrast, the EOF2 pattern (Fig. 10f) resulted from variations in the Kuroshio intrusion over the southwest of Kyushu and off the northeast of Taiwan. Years of positive PC2 are associated with enhanced Kuroshio intrusion. The SSH over the western side of the Kuroshio region increased with the enhanced intrusion onto the ECS shelf. This

EOF2 pattern was not significantly correlated with the local atmosphere forcing (Fig. 10f).

3.3.2. The subsurface

Fig. 11a–d presents the first two EOFs and the associated PCs of subsurface (50 m) currents. These two EOF modes explained 78% of the total variance. The EOF1 pattern presented a change in the intensity of cyclonic circulation in this region. The EOF2 pattern demonstrated the coastal current off the coast of China at approximately 27°N that extended northward approximately along the 70-m isobath.

The significant correlation of the subsurface flow field (black vectors in Fig. 11e) and PC1 revealed a close in-phase relationship with the Kuroshio intrusion. Thus, a favorable correlation was observed between the PC2 of surface current fields and the PC1 of subsurface current fields (correlation coefficient = 0.73). The linear regression map of PC1 in Fig. 11e suggests that the anomalous wind over the Tsushima Strait and the anomalous SSH southwest of the Korean peninsula are directly related to the EOF1 pattern. The absence of a significant relation between PC1 and wind stress curl indicates the divergence or convergence
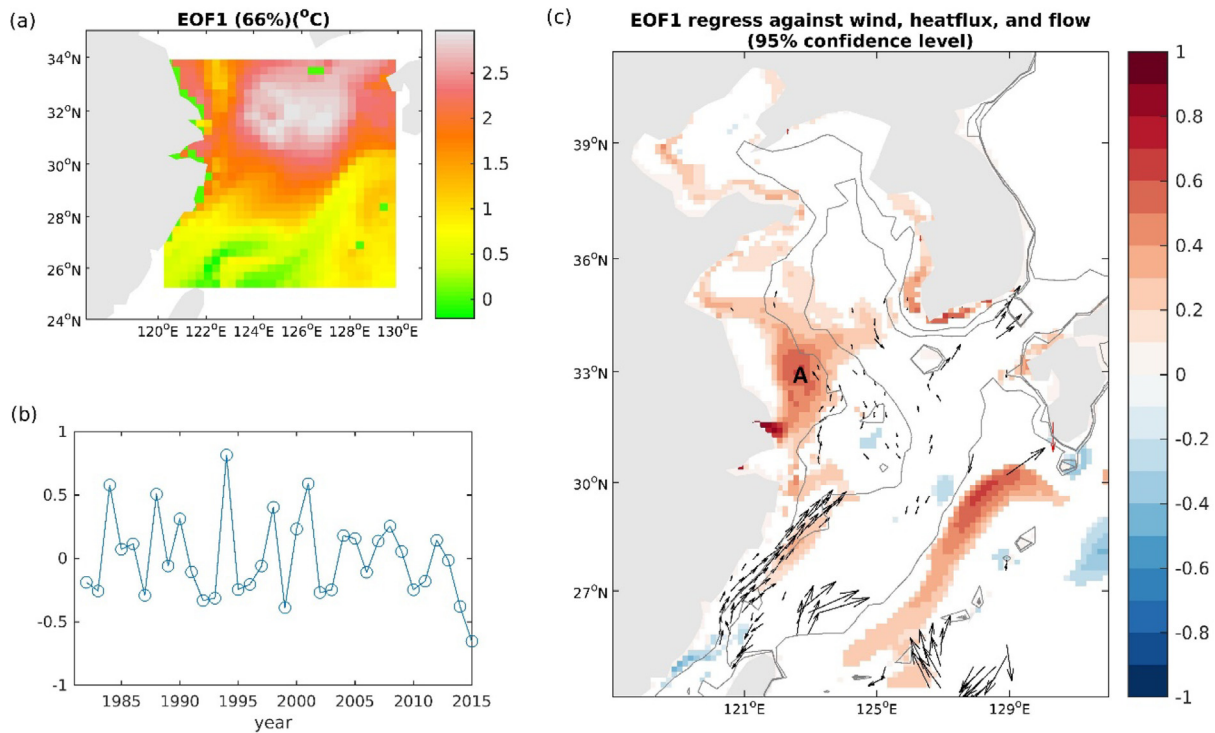
Fig. 8. (Left) The first EOF and its associated PC1 for the July SST. (Right) The regression map of PC1 against surface heat flux (shading, downward flux is positive), wind stress (red vectors), and surface flow (black vectors). Only p < 0.05 is shown. Gray contours are 40, 70 m, and 200 m isobaths, respectively.
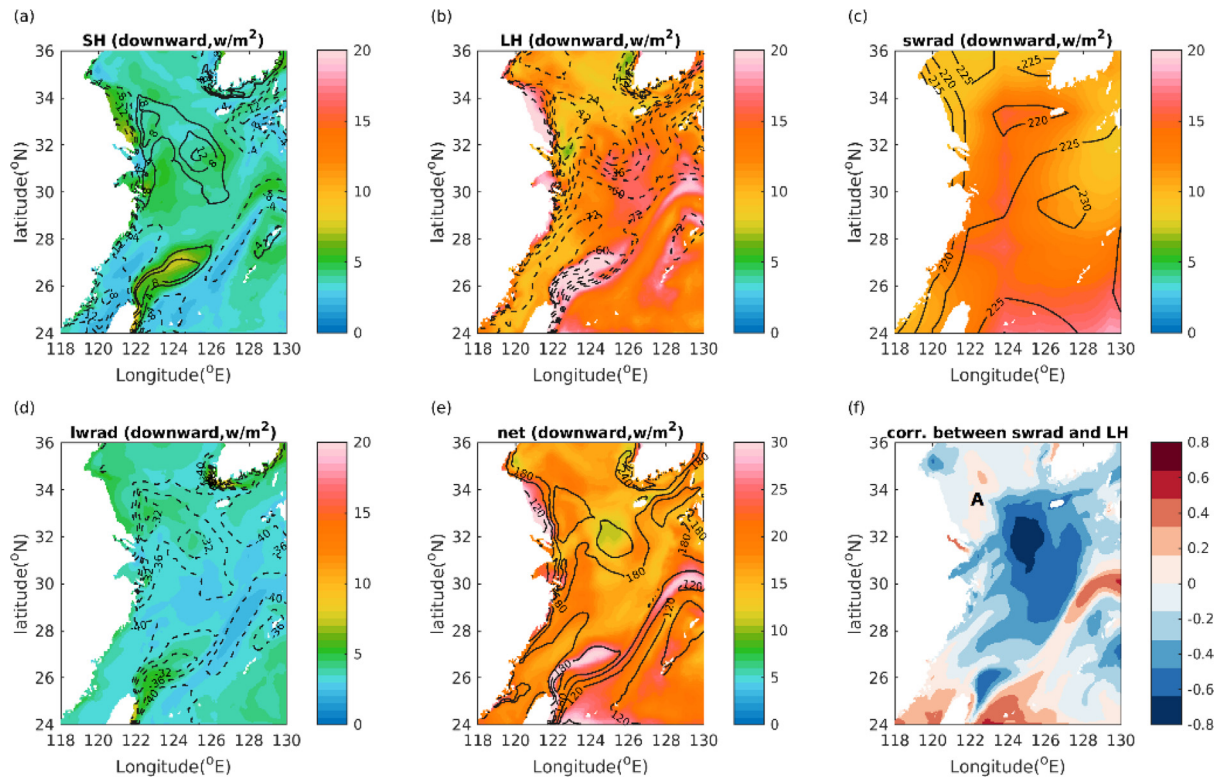

Fig. 9. Climatological mean (black contours) and standard deviation (shaded color) of the modeled surface (a) sensible heat flux, (b) latent heat flux, (c) shortwave radiation, (d) longwave radiation, (e) net heat flux, respectively (downward positive for all fluxes, W/m^2) in July. (e) correlation between the latent heat flux and shortwave radiation.

associated with the SSH anomalies resulting from flow-topography interaction. These results suggest a potential dynamical process for the anomalous subsurface circulation as follows: the anomalous northeasterly winds over the Tsushima strait induced a southwestward pressure gradient in the ECS due to topographical confinement, resulting in positive SSH anomalies around Cheju Island. These anomalies propagated to the south through topographic Rossby waves with shallower bathymetry at their right side. The ocean current anomalies extended
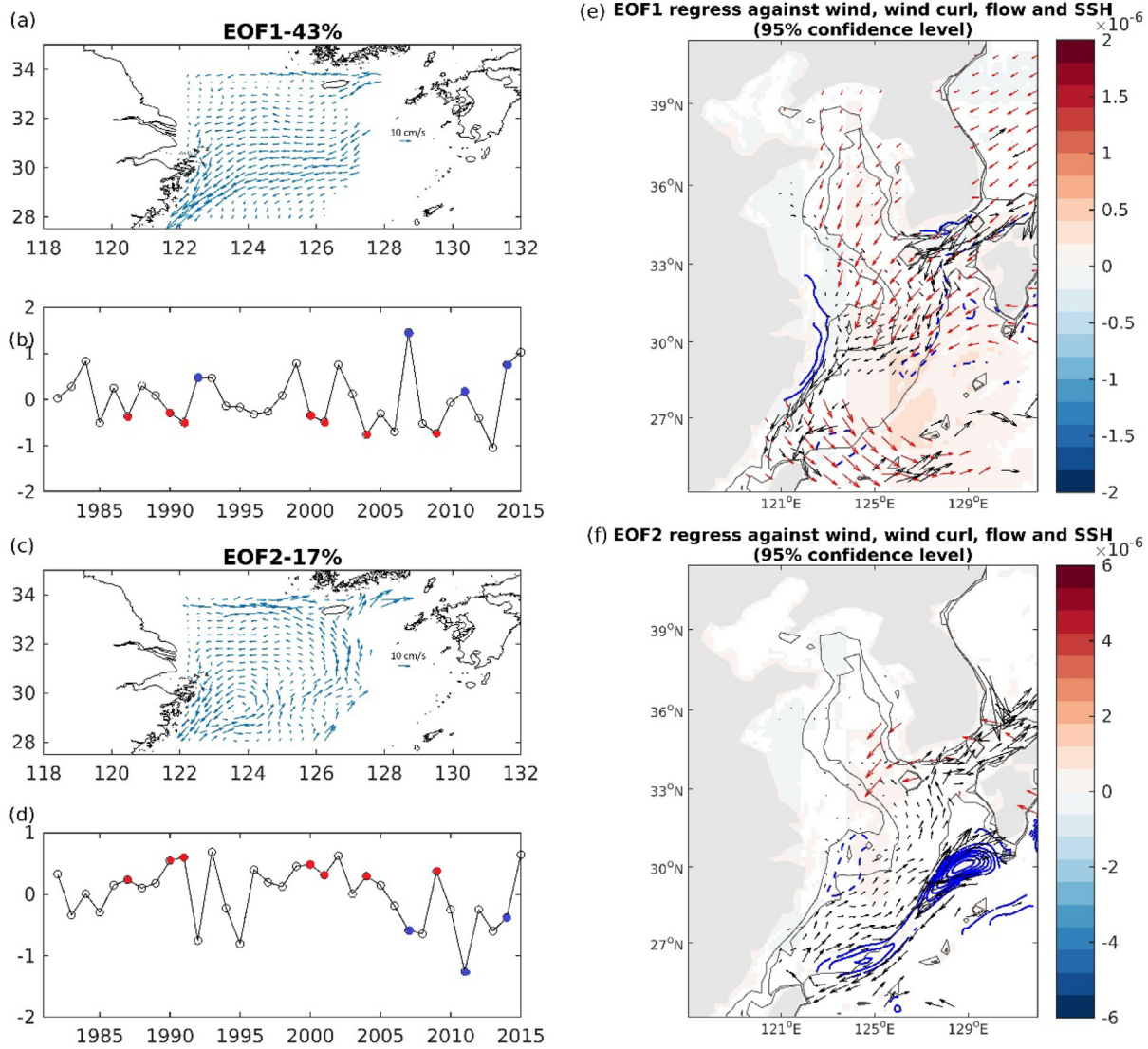
Fig. 10. (a–d) the first two dominant EOFs and their associated PCs for the surface currents. (e–f) the regression map of PCs against SSHs (blue contours), wind stresses (red vectors), wind stress curls (shading), and surface currents (black vectors). Only p < 0.05 is shown. Gray contours are 50, 70 m and 200 m isobaths, respectively. The red and blue points in PC1 mark the type I and II years respectively.

southward to northwestern Taiwan (Fig. 11e). Fig. 12 presents the time series of surface, subsurface current, and surface wind stress anomalies along the 70-m isobath in 2007, 2011, and 2014 (three largest positive phase years of PC1 in Fig. 11b). The anomalies were calculated by subtracting the 35-year climatological mean. During these three summer seasons, the incidents of anomalous wind induced in-phase surface flow variations along the isobath. By contrast, in the subsurface, southward propagating signals were observed along the isobath (magenta arrows in Fig. 12(a), (e) and (i)). For the topographic Rossby wave, the potential vorticity gradient was dominated by bathymetric variations instead of the Coriolis parameter. The baroclinic topographic waves were trapped at the bottom along continental slopes. The bottom pressure torque induced by the pressure difference along the isobaths played a crucial role in driving these waves (Mertz and Wright, 1992). The mean subsurface current in this region (30°N–34°N) flowed meridionally. Because of the geostrophic adjustment associated with SSH anomalies, oscillations in the v-velocity were less prominent.

The subsurface EOF2 presented a coastal current. The associated PC2 was highly correlated with the PC1 of the surface current (correlation = −0.6), suggesting the manifestation of the dominant surface current pattern (surface EOF1). The subsurface PC2 was associated with

anomalous wind off the east coast of China, leading to the anomalous wind stress curl over the ECS (Fig. 11f). The anomalous wind pattern demonstrated the modulation of the East Asian summer monsoon off the east coast of China. As presented in Fig. 11(f), the wind anomalies caused significant SSH anomalies off the China coast at approximately 28°N–30°N, which induced Kelvin waves propagating southward during the geostrophic flow adjustment (Fig. 11f). Furthermore, the subsurface EOF2 pattern is associated with the upwelling process around the Yangtze Estuary region. The PC2 associated with subsurface EOF2 in Fig. 11d correlates well with the upwelling strength defined by the difference in the mean temperature between 30–70 m in a coastal area U1(29°N–31°N and 121°E–123°E) and a central ECS region U2 (28°N–31.5°N and 120.8°E–125°E) in Fig. 11f (correlation coefficient = 0.76). Note that the upwelling feature is not clear in the SST under the effect of the Yangtze River plume.

4. Discussion

The regression of the subsurface PC1 (Fig. 11e) shows that the circulation anomalies were associated with both the anomalous northeasterly wind and the Kuroshio intrusion. To better clarify this, we
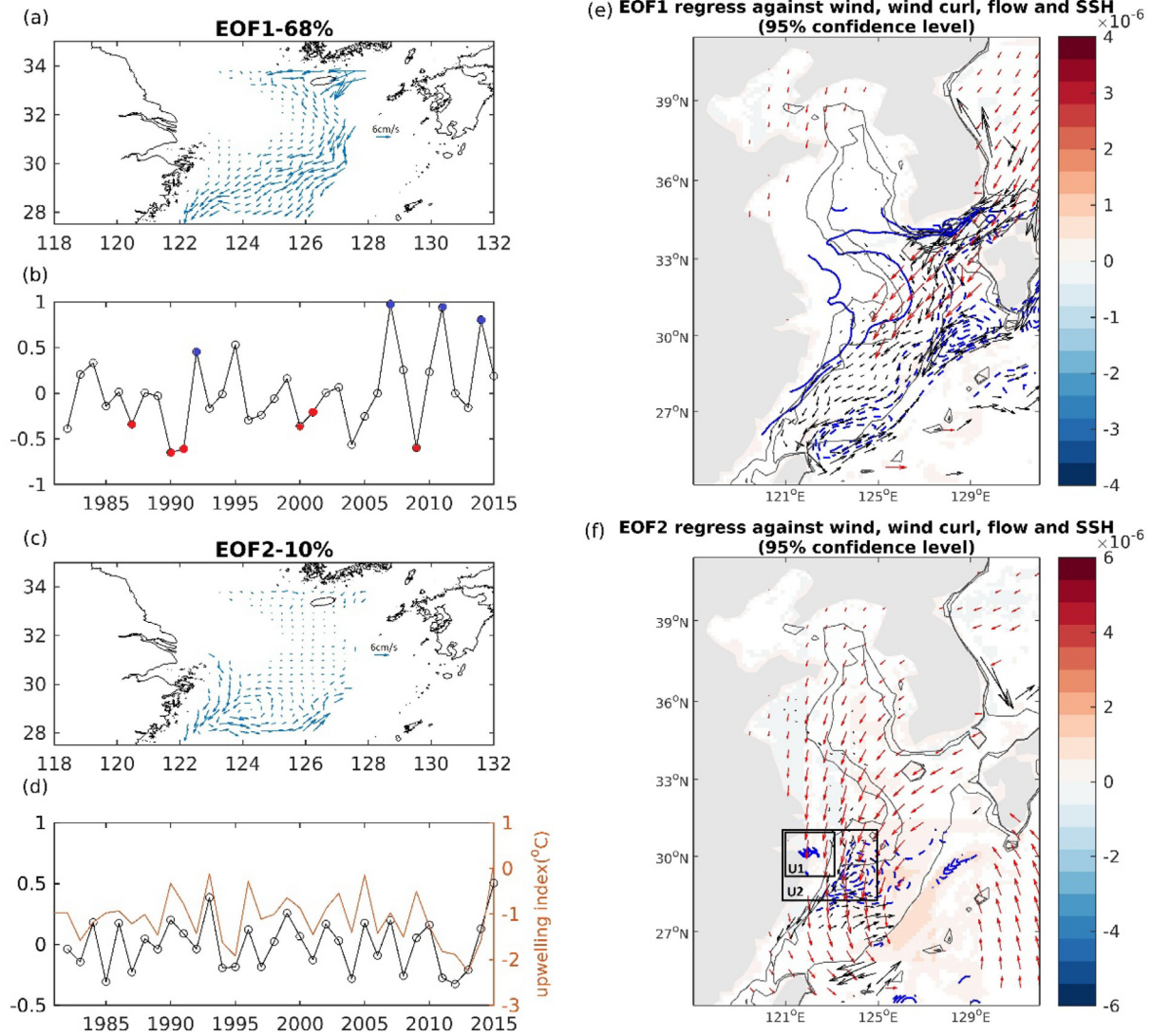
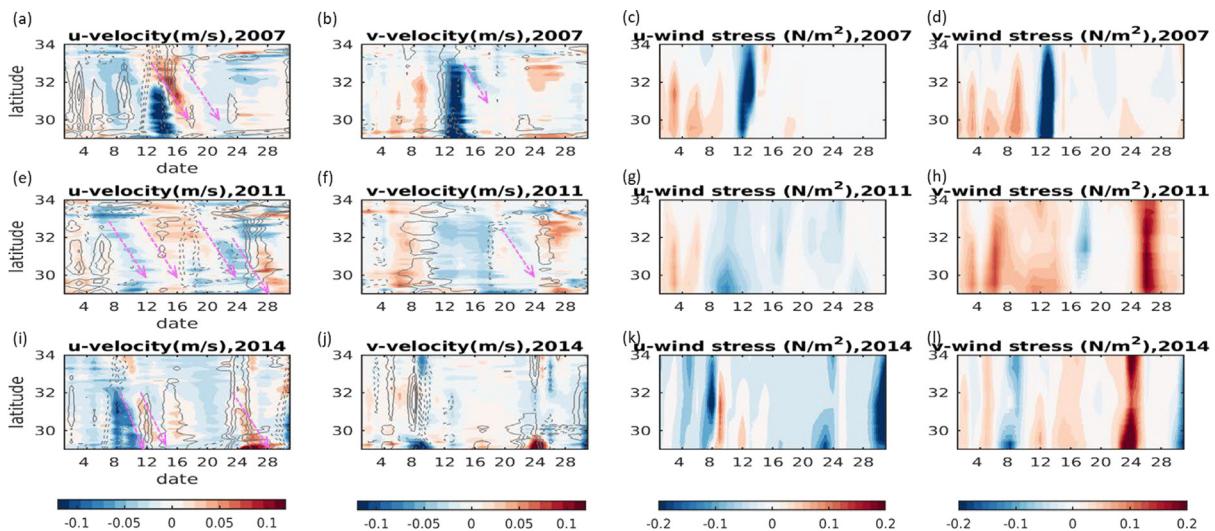**Fig. 11.** Same as Fig. 10 but for the 50 m subsurface currents.

Fig. 12. Time series of surface (contours) and 50 m (shaded color) u, v flow velocity, eastward and northward surface wind stress along the 70 m isobath, for (a)–(d) 2007, (e)–(h) 2011, and (i)–(l) 2014.
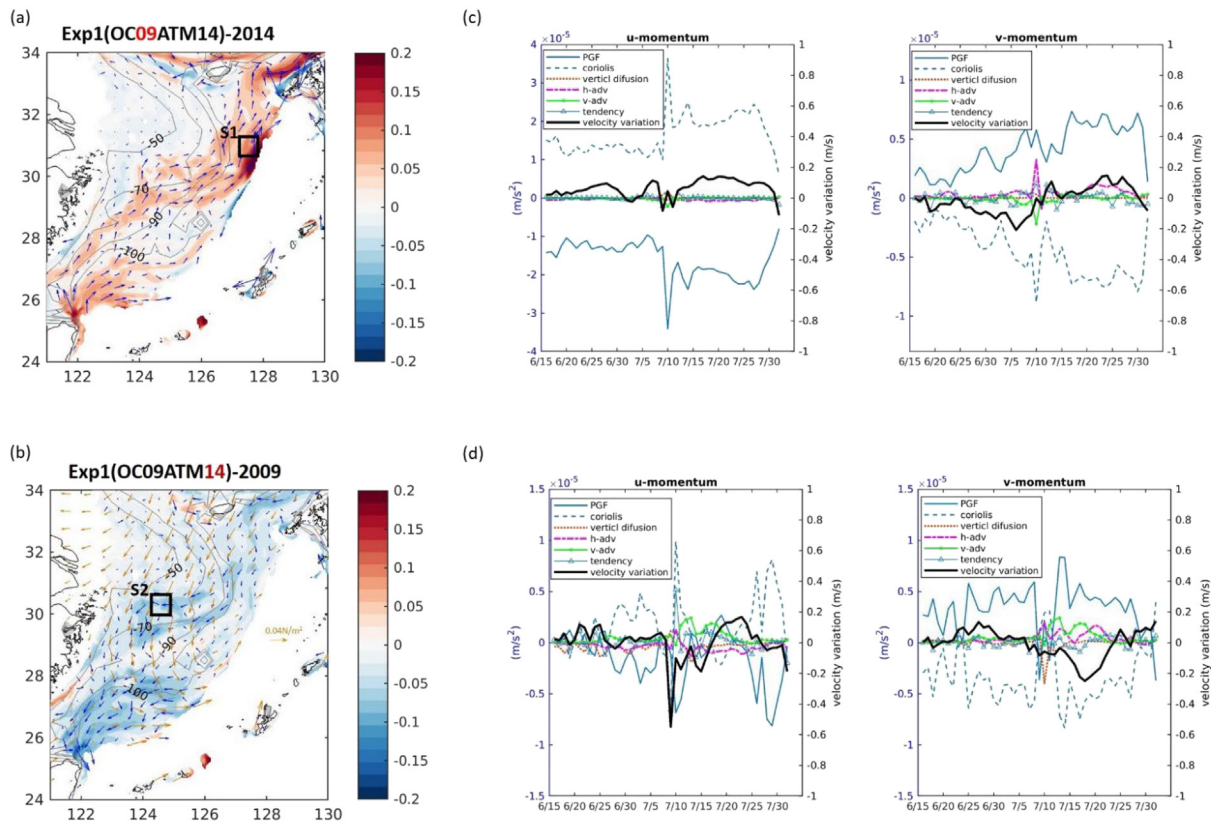
Fig. 13. Subsurface (depth: 30–70 m) mean difference of circulation during July between Exp1 and modeled (a) 2014 (b) 2009 in the 35-yr run. Dark yellow vectors in (b) are the wind stress differences between 2014 and the 35-yr mean. Only region shallower than 200 m-depth was shown. Subsurface momentum budgets averaged in the S1 and S2 regions in Exp1 are provided in (c) and (d), respectively. The black lines are the time-integrated tendency, indicating the variation of each velocity component.

conducted an additional experiment, Exp1, to demonstrate the process associated with different forcings on the variability of subsurface circulation. Among the strong positive phase year of subsurface PC1 (absolute value of PC1 > 0.5), 2009 was a strong Kuroshio intrusion year while 2014 was a strong anomalous northeasterly year. These two years are selected based on the significant Kuroshio mode (EOF2) and the atmospheric wind mode (EOF1), respectively (see Fig. 10). In Exp1, the 2014 atmospheric state is used to force the oceanic states in 2009 (initial and boundary conditions). The circulation differences between Exp1 and the modeled 2014 in the 35-yr simulation shows the influences of the Kuroshio intrusion and the Taiwan Strait inflow with the same atmospheric state (shown in Fig. 13a). In Fig. 13a, there are two sites of the Kuroshio intrusion, one is at around 127°–128°E, and the other is off northeastern Taiwan. The flow modulation is mostly occurred along the 100 m–200 m isobaths and confined to the eastern part of the northern ECS. The enhanced circulation is also contributed by the larger inflow through the Taiwan Strait in the southern ECS. Note that the enhanced intrusion off northeastern Taiwan resulted in the change of flow stream along the China coast. The flow stream moves offshore, causing a negative flow anomaly off the coast. Because of the larger Kuroshio intrusion in the subsurface than the surface, the confinement of the bottom topography on the water column would be more substantial when the Kuroshio intrusion is enhanced. This offshore movement is also presented in the surface EOF2 pattern (the Kuroshio mode).

Furthermore, the differences between Exp1 and the modeled 2009 in the 35-yr simulation show the influence of the anomalous northeasterly subject to the same 2009 ocean state (shown in Fig. 13b). Here, the Kuroshio intrusion and inflow from Taiwan Strait is regarded as remote forcings. The basin-scale wind curls and ocean thermal states control the Kuroshio intensity that fundamentally changes the Kuroshio intrusion into ECS due to JEBAR. The magnitude of flow changes in

Fig. 13b is in the same order as that in Fig. 13a. Compared with Fig. 13a, the change in Fig. 13b is more spatially in-phase since the atmospheric forcing directly acts on the ocean surface. Moreover, the spatial pattern of the circulation anomalies in the northern ECS shows a westward shift. The pressure anomalies induced by the atmospheric winds in the northern ECS could travel to the south through the topography Rossby waves and be trapped in the south allowing energy to accumulate locally.

To better demonstrate the different dynamical processes between the wind induced and the Kuroshio induced modes, Fig. 13c shows the momentum budget averaged within a box (S1 shown in Fig. 13a) in the northeastern ECS in Exp1. Here, the tendency term equals to the sum of the pressure gradient force, Coriolis, horizontal advection, vertical advection, and vertical diffusion terms. The horizontal diffusion is negligible. The black lines show the time-integrated tendency, indicating the variation of each velocity component. In S1, the Kuroshio forcing is dominant. The northward flow change (positive in v-direction) after 6/30 is contributed by the horizontal advection while maintaining the geostrophic balance. Fig. 13d shows the momentum budget averaged in S2 (shown in Fig. 13b) in the inner shelf region in Exp1. In S2, the local wind forcing is dominant. In addition to the vertical diffusion (maximum around 7/9) and horizontal advection, the vertical advection contributes remarkably to the flow change during 7/10-7/20, indicating the breakdown of geostrophic, and the vortex stretching offshore (or squeezing onshore).

In summary, the dynamical processes associated with the distinct wind and Kuroshio intrusion modes are robust features resulting from the direct local and remote forcings, respectively. This is further confirmed by another similar experiment (2007 for wind mode and 2004 for Kuroshio mode). The resulting flows show very similar modulation patterns to those in Exp1 (Fig. 13a–b) (figure not shown). These sensitivity experiments demonstrate the distinct roles of local wind and
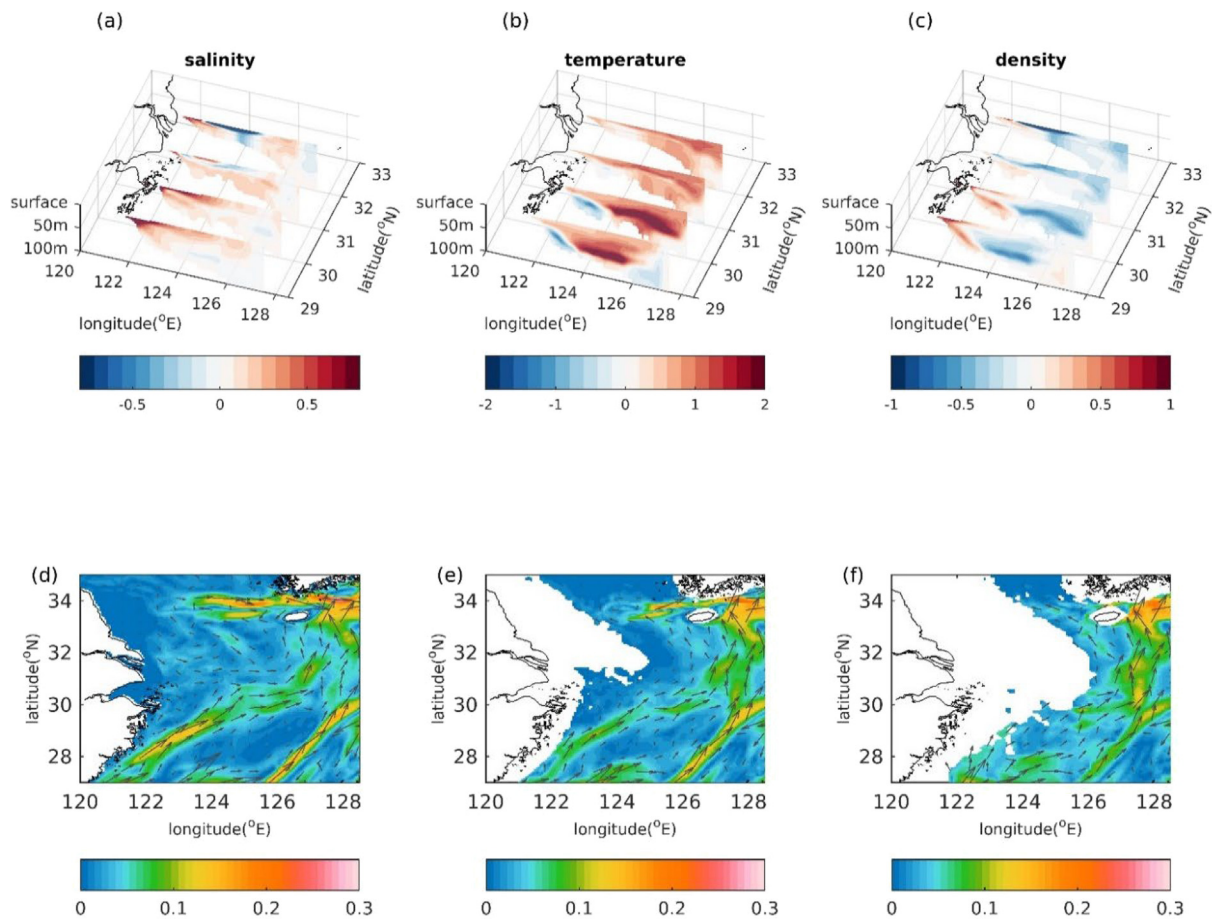
Fig. 14. The composites of Type I (a) salinity (b) temperature (c) density anomaly during July. (d)–(f) anomalous circulation (m/s) at 10 m, 40 m, and 70 m during July, respectively.

remote Kuroshio intrusion on the interannual variability of ECS. The comparison of Exp1 with our long-term simulation is representative regardless of chosen years. Although the sensitivity simulations are only run for two months, the remote/surface forcing directly affect the subsurface and subsurface flow anomalies in the ECS.

5. Summary

We investigated the long-term interannual changes of summer circulation and hydrology in the ECS using 35-year high-resolution ocean model simulation. The SST warming trend was considerably weaker in summer than in winter. To the east of the Yangtze Estuary, the interannual variation of SST in summer was mainly dominated by horizontal advection associated with variations in the Taiwan warm current and heat flux in the offshore region north of the Yangtze Estuary.

The results of EOF analysis demonstrated the presence of the two major types of ocean variability in the ECS (Table 1). Type I is the combination of negative surface and subsurface EOF1, and positive surface EOF2. The combination represents an in-phase contribution between wind and Kuroshio forcing and between the surface and subsurface circulation that enhances the hydrological variability in the ECS. Fig. 14 summarizes the composite anomalies of Type I variability. The eastward flow anomalies at the surface trigger enhanced coastal upwelling accompanied by the increased subsurface Kuroshio intrusion. This modulation favors mixing between the subsurface Kuroshio water and surface diluted water. Higher temperate and salinity anomalies were observed in the area around the Yangtze bank. Over the Yangtze bank, the present negative salinity anomalies were associated with the minimum velocity. Type II is the combination of positive surface and

subsurface EOF1, and negative surface EOF2. The composite anomalies of type I and type II revealed generally opposite patterns. The freshwater in type II was trapped in the Yangtze Estuary region (Fig. 15). For both Type I and II, the surface density and subsurface anomalies were dominated by salinity and temperature, respectively. Overall, these two types of variability represent in-phase relation of the surface and subsurface EOF that enhances the hydrological variability. We note that the typhoons passing by this region have a significant impacts on the upper ocean in summer. These impacts on the surface and subsurface circulations depend heavily on their paths and asymmetrical typhoon wind patterns. Some typhoons with northward trajectories are associated with negative subsurface PC2 (surface PC1) (eg.1987, 1991 and 2006) since the southwesterly winds in the rear half of the typhoons are stronger, while the typhoon with westward moving trajectories (eg.1984 and 2014) could be associated with positive subsurface PC2 (surface PC1) since they bring easterly winds on the right side of the storm tracks. These cases dependent processes may complicate the analysis. The interannual variability of water mass may have large implications for the biogeochemistry change in the ECS. Xu et al. (2019) measured interannual changes in water mass variability in July 2009, 2010, 2011, and 2013 on the mid-shelf of the ECS, suggesting significant effects of circulation change on phytoplankton variability. Their hydrological results in 2009 and 2013 are consistent with Type I anomalies.

Because of the presence of the Yangtze bank and enhanced stratification in the study region, the surface and subsurface EOF modes in circulation may be incoherent. For some years, wind anomalies were observed only in the coastal region of China, resulting in anomalous patterns, which combined surface EOF1 and subsurface EOF2
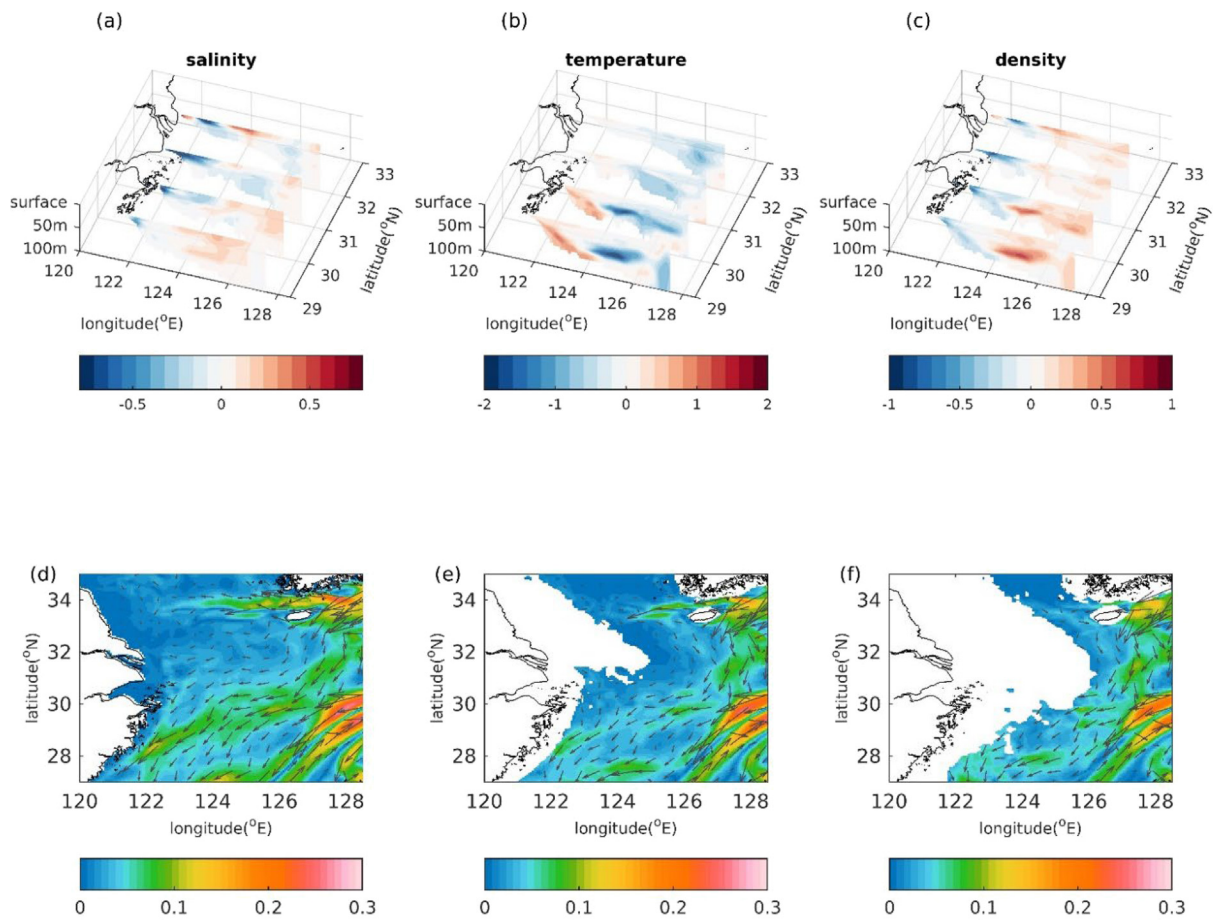
Fig. 15. The composites of Type II (a) salinity (b) temperature (c) density anomaly during July. (d)–(f) anomalous circulation (m/s) at 10 m, 40 m, and 70 m during July, respectively.

Table 1
The 2 types of anomaly based on the EOF results.

Type	Year
I: Surface EOF1$^-$ & Subsurface EOF1$^-$ & Surface EOF2$^+$	1987[a] 1990 1991[a] 2000 2001 2004 2009
II: SurfaceEOF1$^+$ & Subsurface EOF1$^+$ & Surface EOF2$^-$	1992 2007 2011 2014[a]

[a] Years with typhoon events.

(e.g., 2002, 2006, and 2008). In these years, the magnitudes of subsurface flow anomalies were smaller compared with typical Type I and Type II, representing a possibly neutral status.

The variability and its associated cause of summer circulation and hydrology have never been clarified in the ECS. The complex summer current system in the ECS may be governed by local winds, riverine discharge, Kuroshio intrusion, and Taiwan Strait inflow. Using a long-term integration, high-resolution ocean model, we investigated interannual changes in the inner shelf region of the ECS and their dynamics. The summertime sea surface warming was weaker than that in winter due to decreased surface Kuroshio intrusion. To the east of the Yangtze Estuary, variations in local shortwave radiation compensated those in the latent heat flux. Thus, the variation in SST in summer was mainly dominated by horizontal advection associated with the change in the intensity of the Taiwan warm current and the heat flux variation in the shallow region (<40 m) north of the Yangtze Estuary. At the same time, changes in the East Asian summer monsoon modulated surface circulation variability, whereas atmospheric wind anomalies above the Tsushima Strait were associated with changes in subsurface circulation. Enhanced northeasterly winds induced southwestward pressure

gradient anomalies south of the Cheju Island due to topographical confinement. These anomalies may propagate to the south through topographic Rossby waves. The anomalous winds modulated the intensity of coastal upwelling and the Kuroshio intrusion, thus resulting in different types of hydrological anomalies. The type I or type II anomaly indicated the presence of a higher or lower Kuroshio water concentration in the ECS inner shelf. Part of the intruded subsurface Kuroshio water was lifted to the surface layer through coastal upwelling. Differences between the concentration of the Kuroshio water and the distribution of salinity affected the distribution and variation of phytoplankton and thus are crucial for understanding biogeochemical processes and ecosystems in the ECS.

CRediT authorship contribution statement

Yi-Chun Kuo: Formal analysis, Visualization, Writing – original draft. **Yang Yu:** Methodology, Writing – review & editing. **Yu-Heng Tseng:** Conceptualization, Supervision, Methodology, Writing – review & editing.

Declaration of competing interest

The authors declare that they have no known competing financial interests or personal relationships that could have appeared to influence the work reported in this paper.

Data availability

A link to the data has been included at the end of this paper.

Acknowledgments

References

Andres, M., 2008. An Observational Study of the Kuroshio in the East China Sea: Local, Regional, and Basin-Wide Perspectives on a Western Boundary Current. University of Rhode Island.

Berliand, M.E., 1952. Determining the net longwave radiation of the earth with consideration of the effect of cloudiness. Izv. Akad. Nauk. Sssr Ser. Geofiz. 1, 64–78.

Cai, R., Tan, H., Kontoyiannis, H., 2017. Robust surface warming in offshore China seas and its relationship to the East Asian monsoon wind field and ocean forcing on interdecadal time scales. J. Clim. 30 (22), 8987–9005.

Carton, J.A., Chepurin, G.A., Chen, L., 2018. SODA3: A new ocean climate reanalysis. J. Clim. 31 (17), 6967–6983. http://dx.doi.org/10.1175/JCLI-D-17-0149.1.

Chapman, D.C., 1985. Numerical treatment of cross-shelf open boundaries in a Barotropic Coastal ocean model. J. Phys. Oceanogr. 15 (15), 1060–1075.

Chen, C.T.A., 2000. The Three Gorges Dam: reducing the upwelling and thus productivity in the East China Sea. Geophys. Res. Lett. 27 (3), 381–383.

Chen, D., He, L., Liu, F., Yin, K., 2017. Effects of typhoon events on chlorophyll and carbon fixation in different regions of the East China Sea. Estuar. Coast. Shelf Sci. 194, 229–239.

Chen, J., Li, D., Jin, H., Jiang, Z., Wang, B., Wu, B., Hao, Q., Sun, X., 2020. Changing nutrients, oxygen and phytoplankton in the East China sea. In: Changing Asia-Pacific Marginal Seas. Springer, pp. 155–178.

Cheon, W.G., Park, Y.G., Yeh, S.W., Kim, B.M., 2012. Atmospheric impact on the northwestern pacific under a global warming scenario. Geophys. Res. Lett. 39 (16).

Du, X., Liu, J.T., 2017. Particle dynamics of the surface, intermediate, and benthic nepheloid layers under contrasting conditions of summer monsoon and typhoon winds on the boundary between the Taiwan Strait and East China Sea. Prog. Oceanogr. 156, 130–144.

Egbert, G.D., Bennett, A.F., Foreman, M.G.G., 1995. TOPEX/Poseidon tides estimated using a global inverse model. J. Geophys. Res. Oceans 99 (C12), 24821–24852.

Egbert, G.D., Erofeeva, S.Y., 2002. Efficient inverse modeling of barotropic ocean tides. J. Atmos. Ocean. Technol. 19 (2), 183–204.

Emery, W.J., Thomson, R.E., 2001. Data Analysis Methods in Physical Oceanography, second rev. ed. Elsevier, p. 638.

Fairall, C.W., Bradley, E.F., Hare, J.E., Grachev, A.A., Edson, J.B., 2003. Bulk parameterization of air-sea fluxes: Updates and verification for the COARE algorithm. J. Clim. 16 (4), 571–591. http://dx.doi.org/10.1175/1520-0442.

Fairall, C.W., Bradley, E.F., Rogers, D.P., Edson, J.B., Young, G.S., 1996. Bulk parameterization of air-sea fluxes for tropical ocean-global atmosphere coupled-ocean atmosphere response experiment. J. Geophys. Res. Oceans 101 (C2), 3747–3764.

Flather, R.A., 1976. A tidal model of northwest European continental shelf. Mem. Soc. R. Sci. Liege 10.

Goni, G., Kamholz, S., Garzoli, S., Olson, D., 1996. Dynamics of the Brazil-Malvinas Confluence based on inverted echo sounders and altimetry. J. Geophys. Res.: Oceans 101 (C7), 16273–16289.

Guo, X., Miyazawa, Y., Yamagata, T., 2006. The Kuroshio onshore intrusion along the shelf break of the East China Sea: The origin of the Tsushima warm current. J. Phys. Oceanogr. 36 (12), 2205–2231.

Hong, H., Zhang, C., Shang, S., Huang, B., Li, Y., Li, X., Zhang, S., 2009. Interannual variability of summer coastal upwelling in the Taiwan Strait. Cont. Shelf Res. 29 (2), 479–484.

Isobe, A., Matsuno, T., 2008. Long-distance nutrient-transport process in the Changjiang river plume on the East China Sea shelf in summer. J. Geophys. Res.: Oceans 113 (C4).

Johnson, D.R., Boyer, T.P., Seidov, D., Mishonov, A.V., 2015. Regional climatology of the East Asian seas: an introduction. In: Silver Spring: NOAA Atlas NESDIS (2015). p. 79.

Kalnay, E., Kanamitsu, M., Kistler, R., Collins, W., Deaven, D., Gandin, L., Iredell, M., Saha, S., White, G., Woollen, J., 1996. The NCEP/NCAR 40-year reanalysis project. Bull. Am. Meteorol. Soc. 77 (3), 437–472.

Kutzbach, J., 1967. Empirical eigenvectors of sea level pressure, surface temperature, and precipitation complexes over North America. J. Appl. Meteorol. 6, 791–802.

Liu, Z., Gan, J., 2014. Modeling study of variable upwelling circulation in the East China sea: Response to a coastal promontory. J. Phys. Oceanogr. 44 (4), 1078–1094.

Liu, Z., Gan, J., Hu, J., Wu, H., Cai, Z., Deng, Y., 2021a. Progress of studies on circulation dynamics in the East China sea: the kuroshio exchanges with the shelf currents. Front. Mar. Sci..

Liu, Z., Gan, J., Hu, J., Wu, H., Cai, Z., Deng, Y., 2021b. Progress on circulation dynamics in the East China Sea and southern Yellow Sea: Origination, pathways, and destinations of shelf currents. Prog. Oceanogr. 102553.

Liu, C., Wang, F., Chen, X., von Storch, J.S., 2014. Interannual variability of the Kuroshio onshore intrusion along the East China Sea shelf break: Effect of the Kuroshio volume transport. J. Geophys. Res.: Oceans 119 (9), 6190–6209.

Liu, Z.J., Zhu, X.H., Nakamura, H., Nishina, A., Wang, M., Zheng, H., 2021. Comprehensive observational features for the Kuroshio transport decreasing trend during a recent global warming hiatus. Geophys. Res. Lett. 48 (18), e2021GL094169.

Locarnini, R.A., Mishonov, A.V., Antonov, J.I., Boyer, T.P., Garcia, H.E., et al., 2013. NOAA Atlas NESDIS 73 WORLD OCEAN ATLAS 2013 Volume 1: Temperature. Levitus S.Noaa Atlas Nesdis. u.s. Government Printing Office, Wash.d.C.

Medhaug, I., Stolpe, M.B., Fischer, E.M., Knutti, R., 2017. Reconciling controversies about the global warming hiatus. Nature 545 (7652), 41–47.

Mertz, G., Wright, D.G., 1992. Interpretations of the JEBAR term. J. Phys. Oceanogr. 22 (3), 301–305.

Moon, J.H., Kim, T., Son, Y.B., Hong, J.S., Lee, J.H., Chang, P.H., Kim, S.K., 2019. Contribution of low-salinity water to sea surface warming of the East China Sea in the summer of 2016. Prog. Oceanogr. 175, 68–80.

Oey, L.Y., Chang, M.C., Chang, Y.L., Lin, Y.C., Xu, F.H., 2013. Decadal warming of coastal China Seas and coupling with winter monsoon and currents. Geophys. Res. Lett. 40, 6288–6292.

Orlanski, I., 1976. A simple boundary condition for unbounded hyperbolic flows. J. Comput. Phys. 21 (3), 251–269.

Paulson, C.A., Simpson, J.J., 1977. Irradiance measurements in the upper ocean. J. Phys. Oceanogr. 7, 953–956.

Rong, Z., Li, M., 2012. Tidal effects on the bulge region of Changjiang River plume. Estuar. Coast. Shelf Sci. 97, 149–160.

Sakamoto, T.T., Hasumi, H., Ishii, M., Emori, S., Suzuki, T., Nishimura, T., Sumi, A., 2005. Responses of the kuroshio and the kuroshio extension to global warming in a high-resolution climate model. Geophys. Res. Lett. 32 (14).

Sasaki, Y.N., Umeda, C., 2021. Rapid warming of sea surface temperature along the Kuroshio and the China Coast in the East China Sea during the Twentieth Century. J. Clim. 34 (12), 4803–4815.

Shchepetkin, A.F., Mcwilliams, J.C., 2009. Correction and commentary for Ocean forecasting in terrain-following coordinates: Formulation and skill assessment of the regional ocean modeling system by Haidvogel, et al., J. Comp. Phys. 227, 3595–3624. J. Comput. Phys. 228 (24), 8985–9000.

Soeyanto, E., Guo, X., Ono, J., Miyazawa, Y., 2014. Interannual variations of Kuroshio transport in the East China Sea and its relation to the Pacific Decadal Oscillation and mesoscale eddies. J. Geophys. Res.: Oceans 119 (6), 3595–3616.

Tan, H., Cai, R., 2018. What caused the record-breaking warming in East China Seas during 2016? Atmos. Sci. Lett. 19 (10), e853.

Vorosmarty, C.J., Fekete, B.M., Tucker, B.A., 1998. Global river discharge, 1807-1991, V[ersion]. 1.1 (RivDIS). http://dx.doi.org/10.3334/ORNLDAAC/199, Data set. Available online [http://www.daac.ornl.gov] from Oak Ridge National Laboratory Distributed Active Archive Center, Oak Ridge, Tennessee, U.S.A..

Wang, Q., Li, Y., Li, Q., Liu, Y., Wang, Y.N., 2019. Changes in means and extreme events of sea surface temperature in the east china seas based on satellite data from 1982 to 2017. Atmosphere 10 (3), 140.

Wang, F., Meng, Q., Tang, X., Hu, D., 2013. The long-term variability of sea surface temperature in the seas east of China in the past 40 a. Acta Ocean. Sin. 32 (3), 48–53.

Wei, Y., Huang, D., Zhu, X.H., 2013. Interannual to decadal variability of the kuroshio current in the east china sea from 1955 to 2010 as indicated by in-situ hydrographic data. J. Oceanogr. 69 (5), 571–589.

Xu, Q., Sukigara, C., Goes, J.I., do Rosario Gomes, H., Zhu, Y., Wang, S., Shen, A., de Raús Maúre, E., Matsuno, T., Yuji, W., 2019. Interannual changes in summer phytoplankton community composition in relation to water mass variability in the East China Sea. J. Oceanogr. 75 (1), 61–79.

Yang, J., 2007. An oceanic current against the wind: How does Taiwan Island steer warm water into the East China Sea? J. Phys. Oceanogr. 37 (10), 2563–2569.

Yang, D.Z., Huang, R.X., Yin, B.s., Feng, X.R., Chen, H.y., Qi, J.F., Xu, L.j., Shi, Y.l., Cui, X., Gao, G.D., 2018. Topographic beta spiral and onshore intrusion of the Kuroshio Current. Geophys. Res. Lett. 45 (1), 287–296.

Yu, Y., Chen, S.-H., Tseng, Y.-H., Guo, X., Shi, J., Liu, G., Zhang, C., Xu, Y., Gao, H., 2020. Importance of diurnal forcing on the summer salinity variability in the East China Sea. J. Phys. Oceanogr..

Yu, Y., Gao, H., Shi, J., 2017b. Impacts of diurnal forcing on temperature simulation in the Shelf Seas of China. Period. Ocean Univ. China 47 (4), 106–113. http://dx.doi.org/10.16441/j.cnki.hdxb.20160138.

Yu, Y., Gao, H., Shi, J., Guo, X., Liu, G., 2017a. Diurnal forcing induces variations in seasonal temperature and its rectification mechanism in the Eastern Shelf Seas of China. J. Geophys. Res. Oceans 122 (12), 9870–9888. http://dx.doi.org/10.1002/2017JC013473.

Yuan, D., Hsueh, Y., 2010. Dynamics of the cross-shelf circulation in the Yellow and East China Seas in winter. Deep-Sea Res. II 57 (19–20), 1745–1761.

Zhai, W.-d., Zheng, L.-w., Li, C.-l., Xiong, T.-q., Wang, S.-y., 2020. Changing nutrients, dissolved oxygen and carbonate system in the Bohai and Yellow Seas, China. In: Changing Asia-Pacific Marginal Seas. Springer, pp. 121–137.

Zhang, J., Guo, X., Zhao, L., Miyazawa, Y., Sun, Q., 2017. Water exchange across isobaths over the continental shelf of the East China Sea. J. Phys. Oceanogr. 47 (5), 1043–1060.

Zhou, P., Song, X., Yuan, Y., Cao, X., Wang, W., Chi, L., Yu, Z., 2018. Water mass analysis of the East China Sea and interannual variation of Kuroshio subsurface water intrusion through an optimum multiparameter method. J. Geophys. Res.: Oceans 123 (5), 3723–3738.

Zuo, J., Song, J., Yuan, H., Li, X., Li, N., Duan, L., 2019. Impact of Kuroshio on the dissolved oxygen in the East China Sea region. J. Oceanol. Limnol. 37 (2), 513–524.

Zuo, Z., Zhang, R., 2016. Influence of soil moisture in eastern China on the East Asian summer monsoon. Adv. Atmos. Sci. 33 (2), 151–163.

Zweng, M.M., Reagan, J.R., Antonov, J.I., Locarnini, R.A., Mishonov, A.V., et al., 2013. NOAA Atlas NESDIS 74 WORLD OCEAN ATLAS 2013 Volume 2: Salinity. Noaa Atlas Nesdis.